

Alma Mater Studiorum Università di Bologna  
Archivio istituzionale della ricerca

A Novel T6 Rapid Heat Treatment for AlSi10Mg Alloy Produced by Laser-Based Powder Bed Fusion:  
Comparison with T5 and Conventional T6 Heat Treatments

This is the final peer-reviewed author's accepted manuscript (postprint) of the following publication:

*Published Version:*

Di Egidio, G., Ceschini, L., Morri, A., Martini, C., Merlin, M. (2022). A Novel T6 Rapid Heat Treatment for AlSi10Mg Alloy Produced by Laser-Based Powder Bed Fusion: Comparison with T5 and Conventional T6 Heat Treatments. METALLURGICAL AND MATERIALS TRANSACTIONS. B, PROCESS METALLURGY AND MATERIALS PROCESSING SCIENCE, 53, 284-303 [10.1007/s11663-021-02365-6].

*Availability:*

This version is available at: <https://hdl.handle.net/11585/851445> since: 2022-10-05

*Published:*

DOI: <http://doi.org/10.1007/s11663-021-02365-6>

*Terms of use:*

Some rights reserved. The terms and conditions for the reuse of this version of the manuscript are specified in the publishing policy. For all terms of use and more information see the publisher's website.

This item was downloaded from IRIS Università di Bologna (<https://cris.unibo.it/>).  
When citing, please refer to the published version.

(Article begins on next page)

This is the final peer-reviewed accepted manuscript of:

G. Di Egidio et al.

A Novel T6 Rapid Heat Treatment for AlSi10Mg Alloy Produced by Laser-Based Powder Bed Fusion: Comparison with T5 and Conventional T6 Heat Treatments

In: *Metallurgical Materials Transactions B* 53 (2022) 284–303

The final published version is available online at:

<https://doi.org/10.1007/s11663-021-02365-6>

Rights / License:

The terms and conditions for the reuse of this version of the manuscript are specified in the publishing policy. For all terms of use and more information see the publisher's website.

This item was downloaded from IRIS Università di Bologna (<https://cris.unibo.it/>)

**When citing, please refer to the published version.**

# **A novel T6 rapid heat treatment for AlSi10Mg alloy produced by Laser-based Powder Bed Fusion: comparison with T5 and conventional T6 heat treatments**

**Gianluca Di Egidio<sup>1\*</sup>, Lorella Ceschini<sup>1</sup>, Alessandro Morri<sup>1</sup>, Carla Martini<sup>1</sup>,  
Mattia Merlin<sup>2</sup>**

**\* Corresponding author**

<sup>1</sup> Department of Industrial Engineering (DIN), Alma Mater Studiorum, University of Bologna, Viale Risorgimento 4, 40136 Bologna, Italy  
<sup>2</sup> Department of Engineering (DE), University of Ferrara, Via Saragat 1, 44122 Ferrara, Italy

mail: [gianluca.diegidio2@unibo.it](mailto:gianluca.diegidio2@unibo.it), [lorella.ceschini@unibo.it](mailto:lorella.ceschini@unibo.it), [alessandro.morri4@unibo.it](mailto:alessandro.morri4@unibo.it), [carla.martini@unibo.it](mailto:carla.martini@unibo.it), [mattia.merlin@unife.it](mailto:mattia.merlin@unife.it)

## **Abstract**

AlSi10Mg is the most widely studied Al alloy used to produce components by Laser-based Powder Bed Fusion (LPBF), also known as Selective Laser Melting (SLM). Several papers have already investigated the effects of conventional heat treatment on the microstructure and mechanical behavior of the LPBF AlSi10Mg alloy, overlooking, however, the particular microstructure induced by rapid solidification. This paper reports on the effects of a T5 heat treatment and a novel T6 heat treatment on microstructure and mechanical behavior of the LPBF AlSi10Mg alloy, consisting of rapid solution (10 min at 510 °C) followed by artificial aging (6 h at 160 °C). The short solution soaking time reduced the typical porosity growth occurring at the high temperature and led to a homogeneous distribution of fine globular Si particles in the Al matrix. In addition, it limited the diffusion processes, increasing the amount of Mg and Si in solid solution available for precipitation hardening and avoiding the microstructural coarsening. As a result, the strength-ductility balance was improved by increasing both yield strength and elongation to failure, respectively of about 14% and 7% compared with the best solution among those reported in the literature for conventional T6 heat treatment of LPBF AlSi10Mg alloy.

## **Keywords**

Laser Powder Bed Fusion (LPBF), Selective Laser Melting (SLM), Al alloy, AlSi10Mg, heat treatment, microstructure, mechanical properties.

## **1. Introduction**

The AlSi10Mg alloy is currently the most investigated Al alloy in Additive Manufacturing (AM), mainly for the Laser-based Powder Bed Fusion (LPBF) process, also known as Selective Laser Melting (SLM), due to its high AM feasibility [1-3] and positive response to heat treatment [4-6]. These features make it ideally suited to the production of lightweight and thin-walled parts as well as more complex shaped components subjected to high mechanical loads [7-9]. As widely described in the literature, LPBF technology enables components to be produced through a layer-by-layer deposition process [3,7]. The interaction between the laser beam and the material determines the fusion of a localized area, generating a semicircular molten pool, called Melt Pool (MP) [8,9] and the growth of columnar epitaxial grains from the solid substrate during the layer-by-layer deposition process [1,3]. Because of the particular solidification conditions a hierarchical microstructure is formed. Epitaxial solidification and competitive growth promote the formation of a directional microstructure aligned with the direction of maximum thermal flow at the solid/liquid interface [10,11]. The non-equilibrium

solidification conditions into the MP lead to the development of a metastable fine cellular microstructure within the columnar epitaxial grains which are characterized by sub-micrometric cells of supersaturated  $\alpha$ -Al solution surrounded by a eutectic Si network [10-13] and a limited precipitation of  $Mg_2Si$  and Si particles [14,15]. Compared with the Melt Pool Core (MPC), the continuous heating and cooling cycles, necessary for the complete printing of the 3D component, generate a Heat Affected Zone (HAZ) adjacent to the Melt Pool Borders (MPB) where the eutectic Si network appears fragmented and is characterized by the presence of small agglomerated Si particles [11,16]. Moreover, the limited control over material solidification during LPBF leads to the development of defects, such as gas porosities and lack of fusion zones [17-20]. The ultra-fine cellular microstructure, characterizing the as-built AlSi10Mg alloy, leads to the synergistic effect of multiple strengthening mechanisms including: microstructural refinement, solid solution, aggregated second phase (eutectic Si network), high dislocation density and limited precipitation hardening. Consequently, a higher tensile strength is generally obtained, although with lower ductility and toughness, than the as-cast Al alloys [11,14,15,21-23].

As widely reported in the literature, several heat treatments have been recently applied to the as-built AlSi10Mg in order to improve its mechanical properties.

T5 heat treatment (direct artificial aging (AA)), carried out at aging temperature ( $T_{AA}$ ) between 150 and 180 °C and aging time ( $t_{AA}$ ) between 2 and 6 h, is applied to slightly reduce residual stresses and to increase material strength without reducing ductility [15,24,25]. The T5 heat treatment, in fact, does not affect the characteristic as-built microstructure (MP structure, epitaxial grains and cellular sub-structure) but, because of the short diffusion distances of Si atoms from the supersaturated Al lattice, it promotes the formation of acicular nano-sized Si precipitates and  $Mg_2Si$  precursors within the cells of the Al matrix [15,26,27], which lead to an increase in both hardness and tensile strength.

Stress relieving (SR), with an annealing temperature ( $T_{SR}$ ) around 300 °C and time ( $t_{SR}$ ) up to 2 h, is applied to reduce residual stresses and to increase ductility in as-built LPBF AlSi10Mg alloy. After 1 h at 300 °C, in fact, the metastable as-built microstructure evolves towards a more stable condition with the formation of globulized Si particles and the partial disappearance of the MPs, without clear effects on the epitaxial grains. The residual stresses are almost completely relieved [24,28-31], the ductility of the alloy increases, but yield strength and ultimate tensile strength drop [15,27,30].

Conventional T6 heat treatment is carried out with a solution temperature ( $T_{SHT}$ ) between 510 and 550 °C, a solution time ( $t_{SHT}$ ) between 1 and 8 h, an aging temperature ( $T_{SHT}$ ) between 160 and 190 °C, an aging time ( $t_{SHT}$ ) between 4 and 12 h. As a matter of fact, the T6 heat treatment deletes the MP structure, inducing a negligible epitaxial grains growth and forming a more homogeneous composite-like microstructure of Si particles embedded in the  $\alpha$ -Al phase matrix [15,22,32-34]. These changes are promoted by the high temperatures and the long soaking time of the solution step (SHT), which cause firstly the dissolution of the eutectic Si network and then the coalescence of the Si particles due to Si diffusion from the supersaturated  $\alpha$ -Al phase [28,32,35]. In addition, as described by Tonelli et al. [26], the high temperature of the SHT step makes it possible to reduce the anisotropy of the as-built microstructure and to completely relieve residual stresses after only 10 min. Unfortunately, the high solution temperature also leads to the increase of the gas porosities size, due to the expansion of the occluded gas [36,37]. However, during AA the precipitation of

both  $\beta''$  and  $\beta'$  strengthening phases (precursors of the  $\text{Mg}_2\text{Si}$  equilibrium phase) occurs, leading to precipitation hardening [5,32,37]. The T6 heat treatment therefore makes it possible to obtain a balance of the mechanical properties by improving toughness and ductility (thanks to the composite-like microstructure) without inducing a decrease in yield strength (due to the increased contribution of the precipitation hardening) and simultaneously improving the fatigue behavior, as described in [15,23,32,37].

For these reasons, the optimization of the T6 heat treatment parameters and its effects on the LPBF AlSi10Mg alloy are still widely studied. According to most researches [35,37-39], the distribution, size and morphology of the Si particles represent the most important microstructural aspects that influence the mechanical properties of the T6 heat-treated LPBF AlSi10Mg alloy. In their studies Tocci et al. [37] and Wang et al. [6] described the detrimental effects of the coarsening of the Si particles on the strength of the T6 heat-treated alloy. Iturrioz et al. [35] and Mertens et al. [38] also underlined the importance of limiting the Si particle size in order to improve cohesion between the Si particles and the Al matrix, hence increasing the elongation to failure. Zhang et al. [39] suggested that a homogeneous distribution of fine Si particles could lead to a concurrent increase of both the alloy strength and ductility, induced by the higher cohesion between Si particles and Al matrix. Domfarg et al. [33] and Alghamdi et al. [34], in contrast, highlighted the following points: (i) the T6 heat treatment marginally affects the epitaxial grains size and morphology; (ii) the modification of grain size and/or morphology do not induce appreciable effects on the static mechanical response of the LPBF AlSi10Mg alloy.

Based on the above considerations, the strength-ductility trade-off in the T6 heat-treated LPBF AlSi10Mg alloy can be clearly improved by reducing the size and homogenizing the distribution of the Si particles, as well as by avoiding the growth of gas pores during the high temperature solution treatment. Despite this, up to now the research has largely focused on the assessment of the T6 heat treatment effects, carried out with typical parameters used for cast components, without fully investigating possible modification of the solution parameters in order to induce a customized microstructure and therefore to optimize the mechanical properties. To the best of our knowledge, only Li et al. [32] and Iturrioz et al. [35] have systematically studied the influence of solution temperature on LPBF and T6 heat-treated AlSi10Mg alloy, but the effect of a rapid solution (soaking time significantly shorter than 1 h) has not been analyzed yet.

For these reasons, the present work will focus on the development of an innovative T6 rapid heat treatment for LPBF AlSi10Mg alloy, based on a rapid SHT capable of homogenizing the microstructure and relieving the residual stresses of the as-built microstructure, without losing its particular microstructural fineness and the strengthening mechanisms associated with it. Our attention is focused on the effects of the solution temperature and the short soaking time on: (i) size, morphology, and distribution of Si particles; (ii) gas pores size; (iii) Al matrix supersaturation. Understanding these aspects has enabled the definition of customized heat treatment parameters for the LPBF AlSi10Mg alloy, capable of improving the material's strength-ductility balance, based on a new approach for this alloy. To evaluate the achievement of this objective, the tensile properties of the alloy after the new T6 rapid (T6R) heat treatment were compared with the properties of the alloy in the as-built (AB) condition and after a T5 (T5) and T6 benchmark (T6B) heat treatments, considered able to induce in the alloy the best strength-ductility trade-off among those reported in the literature.

However, the influence of the T6R on the residual stresses will be not considered. In fact, the residual stresses have a negligible effect on static mechanical properties [1,3,8] and, more importantly, heat treatments carried out in the range 290 ÷ 540 °C allow the residual stress of the LPBF AlSi10Mg alloy to be almost completely relieved in a short soaking time: 45 min at 290 °C and 10 min at 540 °C [24,26]. Therefore significant differences between the T6R or the T6B tensile strength due to the residual stresses are not expected.

## 2. Experimental

### 2.1 Material and LPBF process

Gas atomized powders of AlSi10Mg alloy, with the nominal chemical composition given in Table 1 and physical properties given in Table 2, were used to produce rod specimens (diameter of 9 mm and height of 77 mm) by LPBF with their longitudinal axis corresponding to the vertical building direction z (Fig. 1.a).

**Table 1.** Chemical compositions (wt%) including: (i) AlSi10Mg powders, supplied by the producer; (ii) rod specimens, evaluated by means of glow discharge optical emission spectroscopy (GD-OES); (iii) the nominal composition of the AlSi10Mg alloy, according to EN AC-43000.

Element (wt%)	Al	Si	Mg	Fe	Cu	Mn	Ni	Pb	Sn	Ti	Zn
<b>Powders</b>	Bal.	9.21	0.27	0.15	0.001	0.006	0.003	0.001	<0.001	0.05	0.002
<b>Rod specimens</b>	Bal.	9.662 ± 0.103	0.285 ± 0.020	0.120 ± 0.017	-	0.006 ± 0.001	-	0.008 ± 0.002	0.025 ± 0.010	0.017 ± 0.003	0.042 ± 0.009
<b>EN AC-43000</b>	Bal.	9±11	0.20±0.45	<0.55	<0.05	<0.45	<0.05	<0.05	<0.05	<0.15	<0.10

**Table 2.** Physical properties of the AlSi10Mg powders supplied by the producer.

Tap density [g/cm <sup>3</sup> ] ASTM B527	Carney Apparent density [g/cm <sup>3</sup> ] ASTM B417	Relative humidity [%]	Static Carney Flow test [s/150g] ASTM B964	Powders range size [μm] ASTM B822, B221, B214
1.8	1.49	4.6%	32	20÷63

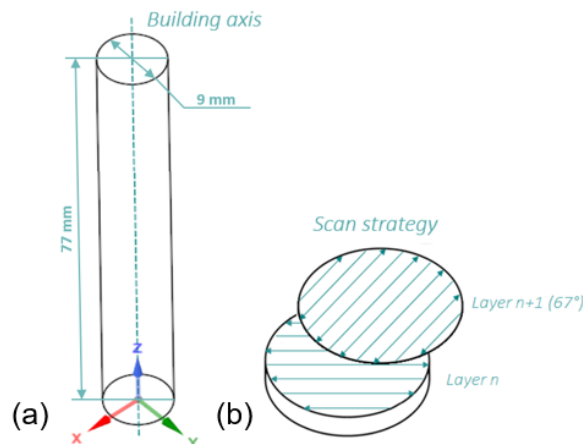


**Fig. 1.** Schematic illustration of the (a) building orientation and (b) scan strategy of the rod specimens.

A SLM500 system (SLM Solution Group AG, DE [41]), including a build chamber of 500x280x365 mm<sup>3</sup> and four Yttrium fiber laser sources (4x400 W) was used for manufacturing the samples. The specimens were fabricated on a heated platform (150 °C) using a bidirectional stripes scan strategy of 67° rotation between subsequent layers (Fig. 1.b) and a re-melted contour zone strategy at the end of each scanning. The build chamber was backfilled with Ar with low oxygen content (<0.2 vol.%). The samples were removed from the platform through wire electrical discharge machining. The LPBF process parameters are reported in Table 3.

**Table 3.** LPBF process parameters set for building AlSi10Mg samples.

Atmosphere	Heated platform [°C]	Laser power [W]	Scan speed [mm/s]	Spot diameter [μm]	Layer thickness [μm]	Hatch distance [μm]	Energy density [J/mm <sup>3</sup> ]
Argon, O <sub>2</sub> <0,2%	150	350	1150	80	50	170	36

Glow Discharge Optical Emission Spectroscopy (GD-OES) was used to check the chemical composition of the as-built specimens (Table 1) according to ISO 14707:2015 [42]. Their composition matched the requirements given by the EN AC-43000 data sheet for AlSi10Mg, also reported in Table 3 for comparison. No significant differences in the composition of the LPBF samples were observed.

## 2.2 Heat treatment and microstructural characterization

The aim of the present study is to identify the optimal T6 heat treatment conditions for the LPBF AlSi10Mg alloy considering its peculiar microstructure. For this reason, a preliminary study was carried out to assess the effect of the heat treatment parameters on the main microstructural features. Thereafter the mechanical performances of the optimized T6R were investigated and compared with those of the alloy in the AB condition and after T5 and T6B heat treatments, as summarized in Table 4.

**Table 4.** LPBF AlSi10Mg alloy heat treatment conditions investigated by tensile test.

Condition	Acronym	Heat treatment
As-built	AB	-
T5 direct artificial aging	T5	(AA) at 160 °C for 4h, air cooling
T6 benchmark heat treatment	T6B	(SHT) at 540 °C for 1h, water quenching at room temperature, (AA) at 160 °C for 4h, air cooling
T6 rapid heat treatment	T6R	(SHT) at 510 °C for 10 min, water quenching at room temperature, (AA) at 160 °C for 6 h, air cooling

The temperatures and soaking times (Table 5) of the SHTs investigated in the present work were defined based on a wide survey of the literature and in particular of the results reported in [25,32,35,43-45]. As the positioning of the samples in the furnace chamber leads to a reduction of its temperature, the soaking time was evaluated from the time when the target value for SHT was reached. Microstructural analyses were carried out after quenching the samples in water at room temperature.

**Table 5.** Investigated SHT conditions for LPBF AlSi10Mg specimens.

Temperature (T <sub>SHT</sub> )	Soaking time (t <sub>SHT</sub> )							
450 °C	-	-	-	-	-	-	60 min	120 min
510 °C	5 min	10 min	15 min	20 min	30 min	60 min	-	-
540 °C	-	-	-	-	-	60 min	-	-

Density measurements were carried out by Archimedes' principle on as-built and solutioned (SHTed) samples (Table 5), according to ASTM B962 [46]. Four samples were analyzed for each condition. To reduce the influence of surface roughness, before the test the specimens were ground by emery papers up to 1200 grits. The weight measurement was repeated three times in air and distilled water. The effective density  $\rho_{eff}$  was elaborated according to the following equation (1):

$$\rho_{eff} = \frac{\omega_{air}}{\omega_{air} - \omega_{water}} \rho_{water} \quad (1)$$

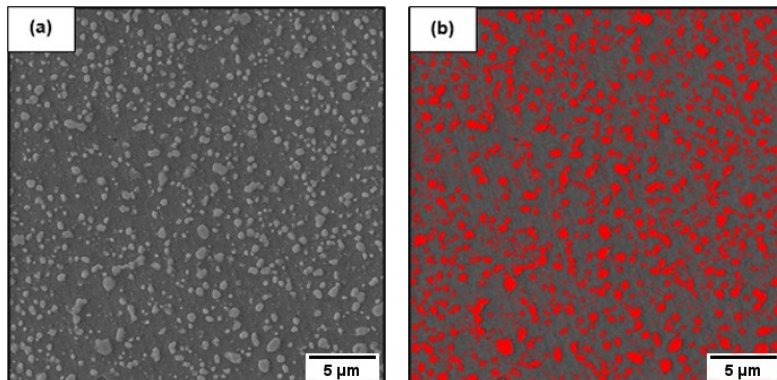
where  $\omega_{air}$  and  $\omega_{water}$  are the weight of the samples in air and in distilled water, respectively. Considering the density of bulk material ( $\rho_{bulk}$ ) equal to 2.68 g/cm<sup>3</sup> for the AlSi10Mg alloy [36], the relative porosity  $P$  in terms of volume percentage was evaluated as follows:

$$P = (1 - \frac{\rho_{eff}}{\rho_{bulk}}).100 \quad (2)$$

X-ray diffraction (XRD) was performed in Bragg-Brentano geometry with a PANalytical X'Pert PRO diffractometer, using a Cu K $\alpha$  radiation source ( $\lambda_{Cu}$ =0.15418 nm). Patterns were acquired in the  $2\theta$  range from 20° to 110° with a 0.02° step size and a 4 s dwell time. After phase identification, a semi-quantitative analysis was carried out to evaluate differences induced by the different heat treatment parameters, by calculating the following: the lattice parameters, the full width at half maximum (FWHM) and the ratio between Si and Al main peak counts [47,48].

Microstructural analyses were carried out on the as-built and heat-treated samples using optical microscopy (OM) and field emission-gun scanning electron (FEG-SEM) microscopy. FEG-SEM was equipped with energy-dispersive X-ray spectroscopy (EDS). Metallographic samples were embedded in conductive resin, ground by emery papers up to 1200 grit, polished by diamond suspensions from 9  $\mu$ m to 1  $\mu$ m, according to ASTM E3 [49] and then etched with Weck's reagent (3g NH<sub>4</sub> HF<sub>2</sub>, 4 mL HCl, 100 mL H<sub>2</sub>O) according to ASTM E407 [50].

Image analysis was carried out by the ImageJ software to identify morphology, size, spatial distribution, and average near-neighbor distance of the eutectic Si particles embedded in the Al matrix. For each solution condition, five FEG-SEM images were analyzed for a total area of about 4x10<sup>-3</sup> mm<sup>2</sup>. The image analysis procedure included the microstructure tessellation by a particle surface-based algorithm into a mesh of Voronoi cells (ImageJ plug-in), each containing an individual particle, as suggested by Li et al. [51]. The Voronoi tessellation allowed the division of the analyzed region into sub-regions so that each Si particle was associated with an area that is closer to it than to any other. This makes it possible to estimate the average nearest-neighbor distance among the Si particles [51]. The analysis process was standardized to guarantee repeatable results. The FEG-SEM images (Fig. 2.a) were elaborated through a threshold function to identify the Si particles (Fig. 2.b). Subsequently, the images were processed to define the Voronoi tessellation resulting from Si particle distribution (Fig. 2.d) and the average nearest-neighbor distance for each image was calculated. Particular attention was paid to different quantitative parameters: (i) average area of Si particles; (ii) Si particle number per unit area; (iii) average near-neighbor distance.





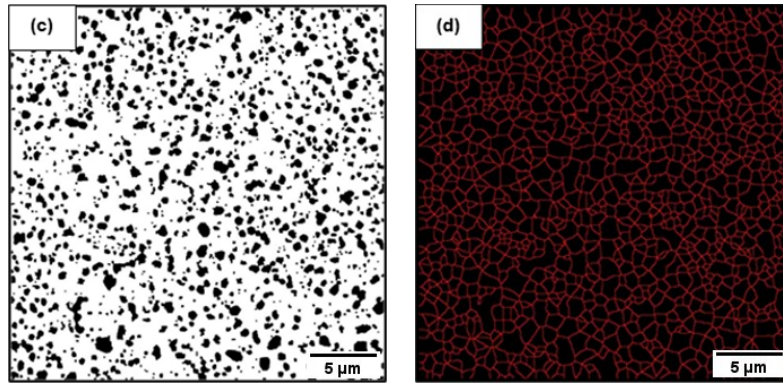


**Fig. 2.** Example of the image analysis processing path comprising: (a) the original FEG-SEM image; (b) identification of Si particles by threshold function; (c) conversion into binary image; (d) the Voronoi tessellation (red lines define the average nearest-neighbor distance for each Si particle).

From the results of the microstructural characterization,  $T_{\text{SHT}}=510\text{ }^{\circ}\text{C}$  and  $t_{\text{SHT}}=10\text{ min}$  were identified as the best temperature and time for the SHT and hereafter referred to as SHTR. This short solution treatment was applied to the samples that underwent further artificial aging and the subsequent mechanical characterization.

Artificial aging (AA) curves were evaluated for both AB and SHTR alloys according to the temperature-time conditions listed in Table 6. Vickers hardness ( $HV_1$ ) tests were performed on the heat-treated samples, according to ASTM E92 [52], to determine hardness as a function of aging time and temperature.

**Table 6.** Artificial aging conditions for T5 and T6R heat treatments

Initial alloy condition	Heat treatment	Artificial aging conditions	
		Temperature ( $T_{\text{AA}}$ )	Soaking time ( $t_{\text{AA}}$ )
As-built (AB)	T5	160 °C/170 °C/180 °C	1÷8 h
Solution treated (SHTR) and quenched (510 °C for 10 min)	T6R	160 °C/170 °C/180 °C	1÷10 h

## 2.3 Mechanical characterization

Tensile and  $HV_1$  hardness tests were performed on samples that underwent different heat treatments. Each tested condition was reported in Table 4. Round dog-bone tensile samples (gauge length  $L_0 = 25\text{ mm}$ , gauge diameter  $d_0 = 5\text{ mm}$ ) were machined from the heat-treated specimens (Fig. 3). Tensile tests were carried out at room temperature on a screw-testing machine at a strain rate of  $3.3 \times 10^{-3}\text{ s}^{-1}$  according to ISO 6892-1 and ISO 6892-2 [53,54]. Yield strength (YS), ultimate tensile strength (UTS) and elongation to failure ( $\epsilon_f$ ) were evaluated as the average of at least four samples for each investigated condition.

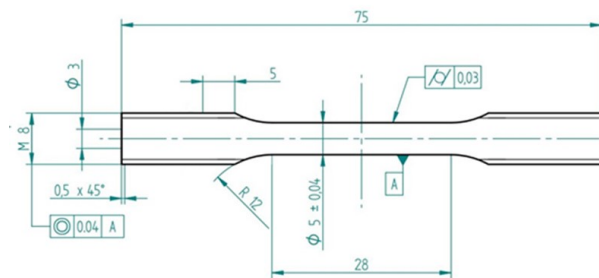


**Fig. 3.** Tensile sample geometry (dimensions in mm).

## 3 RESULTS

### 3.1 Density measurement

Density measurements were carried out on each specimen before and after the solution step to evaluate the effect of SHT on the gas porosity content. This porosity is mainly due to the protective gases (such as Ar or N<sub>2</sub>) used in the building chamber and the H<sub>2</sub> present in moisture on the powder surface. The average density of the as-built samples was 2.656±0.003 g/cm<sup>3</sup> with a consequent porosity content of 0.91%. The average increase of the porosity induced by different T<sub>SHT</sub> and/or different t<sub>SHT</sub> is reported in Fig. 4. These data clearly show that porosity content rises with an increase in both solution temperature and time. Compared with the amount of porosity in the AB samples, at 510 °C the porosity increases from 13.3% after 5 min to 31.6% after 1 h of t<sub>SHT</sub>, whereas for 1 h of solubilization the porosity increases from 18.6% at 450 °C to 40% at 540 °C. The latter represents the worst possible analyzed SHT condition, leading to the highest porosity content. As expected, the increase of porosity is more affected by T<sub>SHT</sub> than t<sub>SHT</sub>. As a matter of fact, at high temperature the gas pressure in the pores increases, the alloy strength decreases and consequently porosities can grow [43,44]. However, on the basis of these results, it is possible to infer that SHT at 510 °C, with soaking time ,of up to 15 min, is able to limit the porosity content increase.

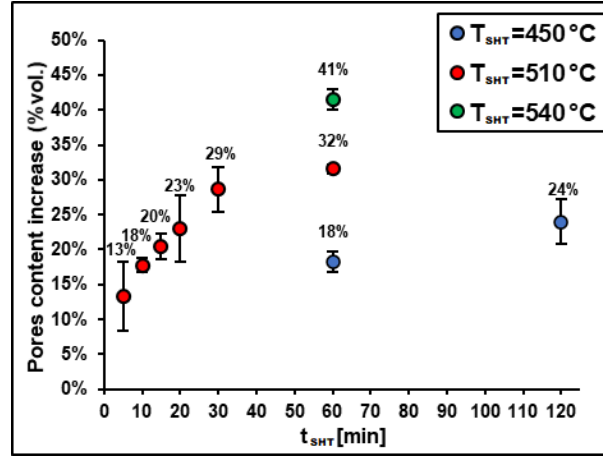


Fig. 4. Effect of T<sub>SHT</sub> and t<sub>SHT</sub> on the increase of pores content in the heat-treated compared with the AB samples.

### 3.2 X-ray diffraction

The main parameters derived from XRD patterns of LPBF AlSi10Mg alloy are summarized in Table 7 and Figure 5, as a function of different SHT conditions. The Si/Al ratio was determined by equation 3, as the ratio between the area under the Si <111> peak and the Al <111> peak,

$$\frac{Si}{Al} = \frac{Area_{Si<111>}}{Area_{Al<111>}} \quad (3)$$

while the effect of the different SHT conditions on the amount of the Si dissolved in Al, was assessed by means of Vergard's law (4) [55]:

$$a = -0.0174x_{Si} + 0.40491 \quad (4)$$

where *a* is the lattice parameter of FCC Al and X<sub>Si</sub> is the atomic fraction of dissolved Si.

FCC Al and diamond cubic Si phases were identified in the XRD patterns of all the samples, with lower intensity for Si than for Al. FCC Al reflections were always sharp, indicating the presence of large crystallites, while no texture was observed. As reported by [10], in fact, the bidirectional stripes scan strategy of 67° rotation between subsequent layers, the large hatch distance (170 μm) and the high layer thickness (50 μm)

used for the production of the LPBF samples can lead to the absence of texture, conversely from unidirectional or bidirectional scan strategy.

The Si FWHM values indicate the presence of finer Si crystallites in AB than in the heat-treated alloy, due to the high cooling rate during LPBF, as also observed by [56]. Among the SHTed specimens treated at 510 °C, those that underwent the shorter solution time of 5 and 10 min have a higher FWHM than the others, due to the retention of smaller Si crystallites. The FWHM of these samples is also broader compared with that of SHT specimens which underwent low  $T_{SHT}$  (450 °C), but longer  $t_{SHT}$  (1+2 h). For  $t_{SHT}$  equal to 1 h, the FWHM decreases, and the Si/Al ratio increases with rising  $T_{SHT}$ , indicating an increase of eutectic Si particle size and amount, respectively. These data agree with the results of microstructural analyses reported in the following sections.

**Table 7.** Si <111> peak FWHM and Si/Al ratio for AB and SHTed samples.

Heat Treatment	$T_{SHT}$ [°C]	$t_{SHT}$ [min]	Si <111> FWHM	Si/Al	$X_{Si}$ [%]
None (AB)	-	-	0.394	0.08	4.17
SHT	450	60	0.148	0.13	3.14
SHT	450	120	0.148	0.25	2.81
SHT	510	5	0.197	0.02	5.90
SHT	510	10	0.197	0.03	6.90
SHT	510	15	0.148	0.04	5.56
SHT	510	20	0.148	0.08	4.55
SHT	510	30	0.148	0.14	3.64
SHT	510	60	0.148	0.15	3.34
SHT	540	60	0.148	0.19	3.34

The plot in Figure 5 clearly shows that the highest amount of Si dissolved in Al ( $X_{Si}$ ) is present in the samples subjected to SHTR for 10 min at 510 °C, while longer  $t_{SHT}$  leads to a decrease of Al saturation. However, as expected, the lowest amount of Si in solid solution was detected in the aged samples ( $X_{Si} = 0.19$  at.% for T6R). Hence the aging treatment, as expected, led to the formation of  $Mg_2Si$  hardening precipitates and to the consequent reduction of the Si supersaturation in the Al-rich matrix [22].

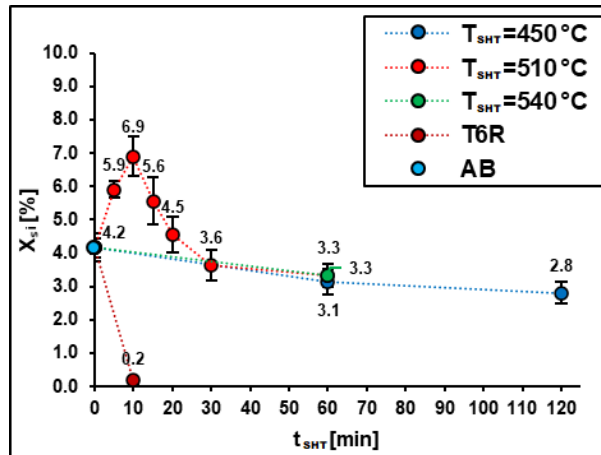
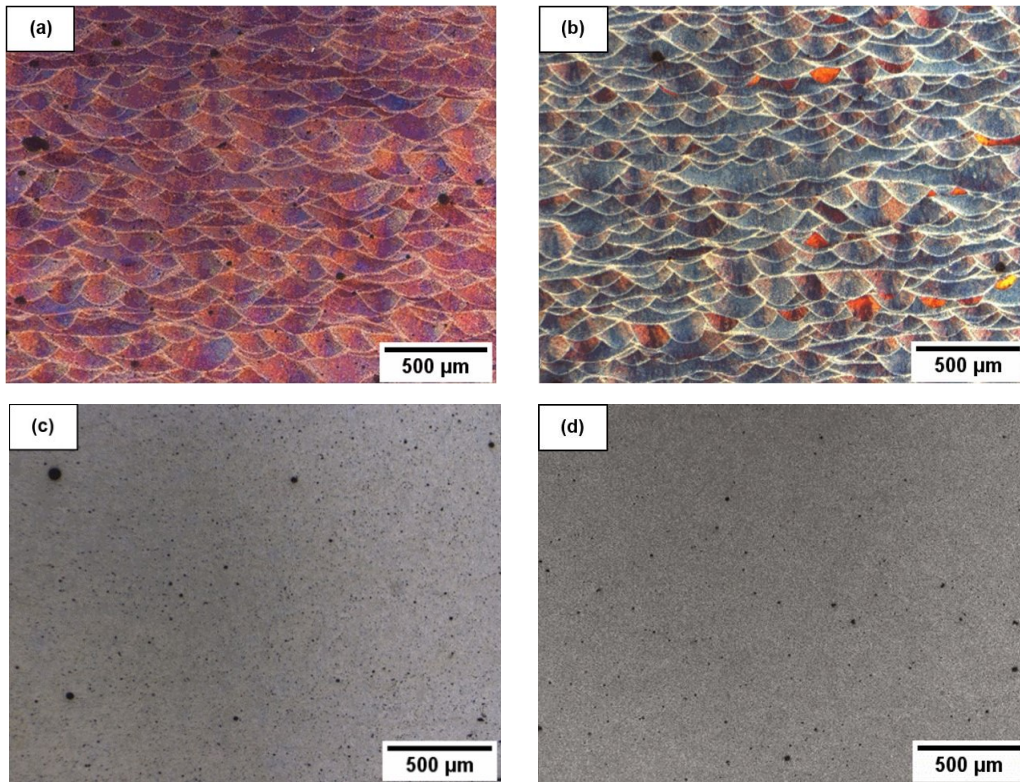


**Fig. 5.** Amount of Si dissolved in FCC Al ( $X_{Si}$ ) estimated by Vergard's law for SHTed samples with different  $T_{SHT}$  and  $t_{SHT}$  and for a T6R heat-treated sample.

### 3.3 Microstructure

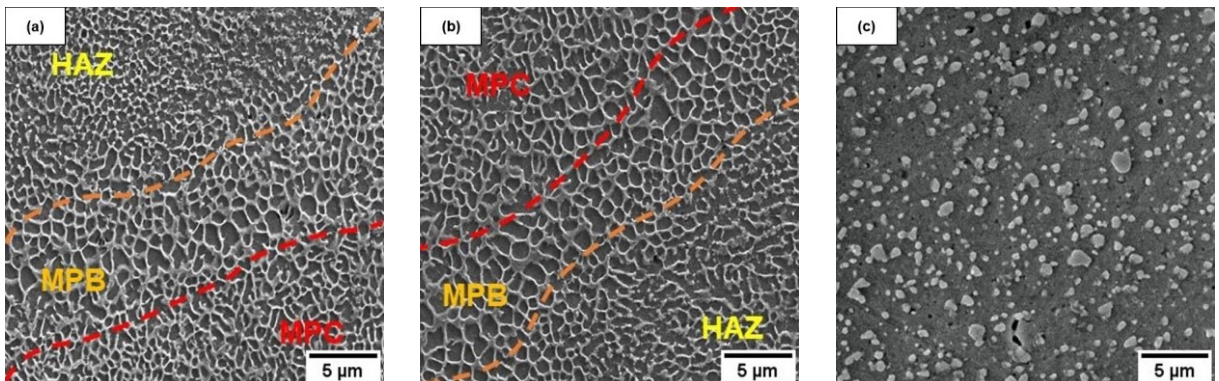
The microstructural analyses aimed to identifying the optimal solubilization conditions by comparing the effect of different heat treatments on MP structure, cellular microstructure, porosity, as well as size, amount and distribution of Si particles.

The OM images reported in Figure 6 clearly show the evolution of the MP structure as a function of the heat treatment temperature. The T5 heat treatment ( $T_{AA}=160\text{ }^{\circ}\text{C}$ ,  $t_{AA}=4\text{ h}$ ) has no remarkable effect (Fig. 6.b) on the MP structure characterizing the AB samples (Fig. 6.a). The diffusion processes at the aging temperatures (in this study ranging between 160 and 180  $^{\circ}\text{C}$ ) are negligible and consequently their effects on the microstructure are negligible too [15,24,27]. The microstructure, in contrast, is clearly affected by the SHT, as evident in Figures 6.c and 6.d. In SHTed samples the MP structure disappears, leading to similar homogeneous microstructures both in the samples subjected to the benchmark solution treatment (SHTB) used to the T6B heat treatment (Fig. 6.c) and the SHTR (Fig. 6.d).



**Fig. 6.** OM images of LPBF AlSi10Mg microstructure: (a) AB; (b) T5:  $T_{AA}=160\text{ }^{\circ}\text{C}$   $t_{AA}=4\text{ h}$ ; (c) T6B:  $T_{SHT}=540\text{ }^{\circ}\text{C}$   $t_{SHT}=1\text{ h}$ ,  $T_{AA}=160\text{ }^{\circ}\text{C}$   $t_{AA}=4\text{ h}$ ; (d) T6R:  $T_{SHT}=510\text{ }^{\circ}\text{C}$   $t_{SHT}=10\text{ min}$ ,  $T_{AA}=160\text{ }^{\circ}\text{C}$   $t_{AA}=6\text{ h}$ . The T5 heat treatment did not affect the MP structure that was instead completely deleted by the SHTR and conventional SHT.

Fuller investigations on the effect of different  $T_{SHT}$  and  $t_{SHT}$  on the microstructure evolution were carried out by FEG-SEM (Fig. 7).





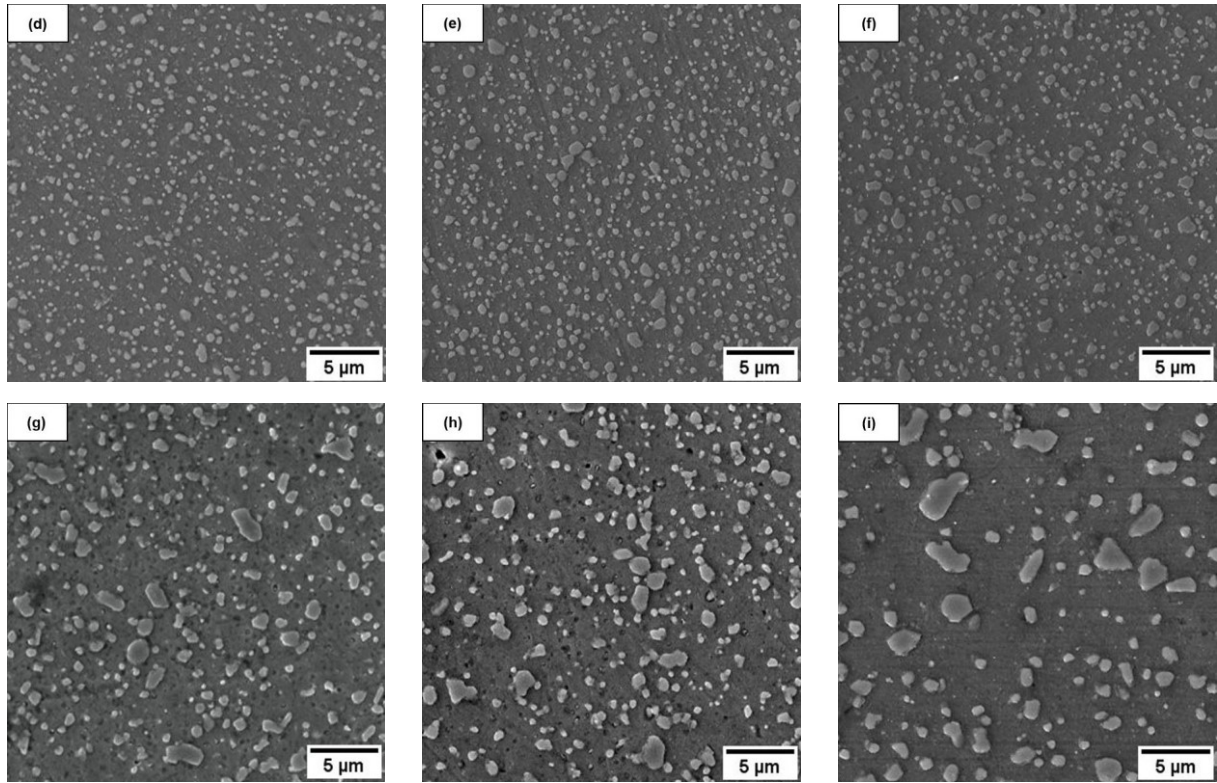


**Fig. 7.** LPBF AlSi10Mg microstructures: (a) AB; (b) T5:  $T_{AA}=160\text{ }^{\circ}\text{C}$   $t_{AA}=4\text{ h}$ ; after solution phase: (c)  $T_{SHT}=450\text{ }^{\circ}\text{C}$   $t_{SHT}=1\text{ h}$ ; (d)  $T_{SHT}=510\text{ }^{\circ}\text{C}$   $t_{SHT}=5\text{ min}$ ; (e)  $T_{SHT}=510\text{ }^{\circ}\text{C}$   $t_{SHT}=10\text{ min}$ ; (f)  $T_{SHT}=510\text{ }^{\circ}\text{C}$   $t_{SHT}=15\text{ min}$ ; (g)  $T_{SHT}=510\text{ }^{\circ}\text{C}$   $t_{SHT}=30\text{ min}$ ; (h)  $T_{SHT}=510\text{ }^{\circ}\text{C}$   $t_{SHT}=1\text{ h}$ ; (i)  $T_{SHT}=540\text{ }^{\circ}\text{C}$   $t_{SHT}=1\text{ h}$ .

In the AB and T5 samples the particular solidification conditions led to the formation of sub-micrometric cells of supersaturated  $\alpha$ -Al solution surrounded by a eutectic Si network (Fig. 7.a and 7.b). The figures show both equiaxed and uniform cells in correspondence with the MPC and coarser and elongated cells next to the MPB, as described in [13-17]. Moreover, at higher magnification (Fig. 8), the presence of acicular nano-sized Si precipitates within the cells of the Al matrix is clearly visible, both in the AB and T5 samples. Their formation is induced by the prolonged exposure to high temperature, due to the use of a heated platform ( $150\text{ }^{\circ}\text{C}$  for 30 h), while the following artificial aging ( $160\text{ }^{\circ}\text{C}$  for 4 h) did not have remarkable effects on Si precipitate size and distribution [15,25].

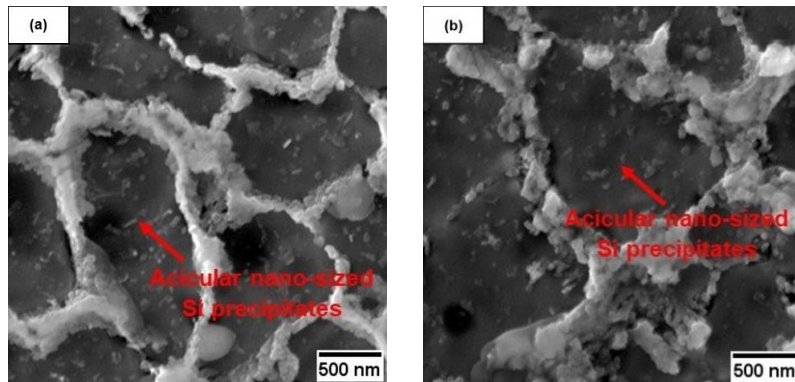


**Fig. 8.** LPBF AlSi10Mg alloy microstructures: (a) AB; (b) T5:  $T_{AA}=160\text{ }^{\circ}\text{C}$   $t_{AA}=4\text{ h}$ .

During SHT, the AB microstructure evolved from the ultrafine cellular structure to a composite-like microstructure of eutectic Si particles embedded into the  $\alpha$ -Al matrix (Fig. 7.c to 7.k). The dissolution of the eutectic Si network and the nucleation of the first nano-sized Si particles can take less than 5 min at high temperature (Fig. 7.e). However, the final size and distribution of the Si particles is a function of both  $T_{SHT}$

and  $t_{\text{SHT}}$  in agreement with the findings of [6,32,35,39], confirming the importance of Si diffusion processes in the particle growth and coalescence.

To carefully assess the effects of SHT conditions on the microstructure, and thereafter on the mechanical properties, a complete image analysis of the Si particles was carried out. Figure 9 shows the average area of the Si particles (Fig. 9.a) and their number per unit area (Fig. 9.b) for each solution condition. The lowest Si particle area and the highest density of Si particles per unit area was observed for SHT carried out at  $T_{\text{SHT}}$  of 510 °C and for  $t_{\text{SHT}}$  in the range of 5÷15 min, indicating that a very short SHT leads both to smaller and more homogeneously distributed Si particles in the Al matrix, as also confirmed by their lower distance (Tab. 8).

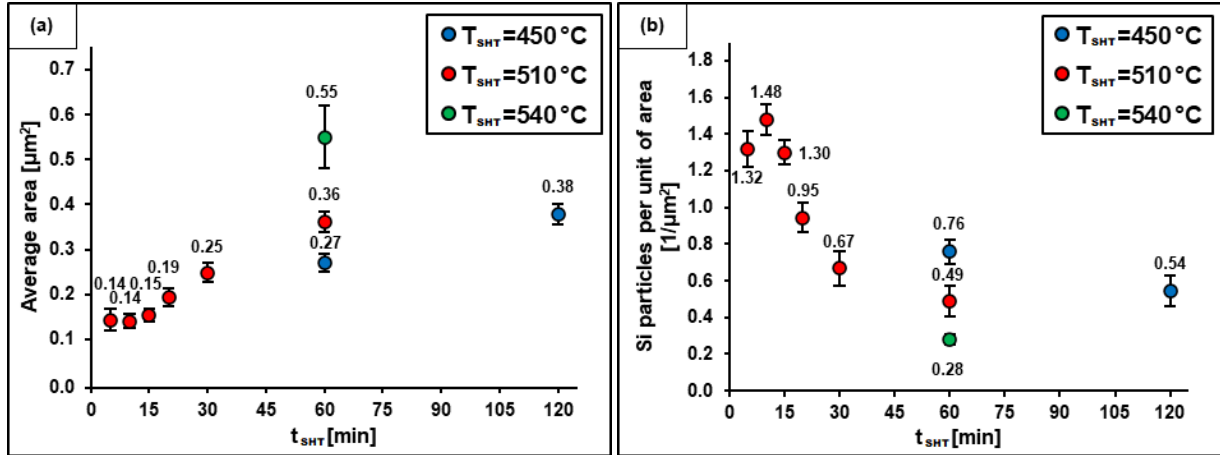


Fig. 9 Effects of different SHT conditions on: (a) Si particle average area; (b) number of Si particles per unit of area.

As reported by Chen [21], reducing the inter-particle distance can induce an increase of the alloy strength contributed by Orowan looping in polycrystalline metals due to the higher stress required to unlock dislocations motion through the nano and micrometric Si particles [34,57-59]. Accordingly, Si particle size and distribution also play a key role in the strengthening process of the alloy. The increase of stress is mainly due to the Orowan strengthening mechanism and can be estimated by the following equation:

$$\Delta\sigma = \frac{MGb}{\lambda} \quad (5)$$

In equation (5),  $M$  is the Taylor factor (3.06 for FCC crystals),  $G$  is the shear modulus (25.4 GPa for Al),  $b$  is the Burger's vector (0.286 nm for Al) and  $\lambda$  is the inter-particle spacing ( $\mu\text{m}$ ) [21]. The results reported in Table 8 clearly show the correlation between a more homogeneous distribution of Si particles into the Al matrix and a higher strengthening level due to dispersed second phases. Table 8 reports the increased strength due to the Orowan mechanism, evaluated for each SHT condition, and the comparison with SHTB ( $T_{\text{SHT}}=540^\circ\text{C}$  and  $t_{\text{SHT}}=1\text{ h}$ ), to focus on the increased strength introduced by the finer microstructure and to minimize possible systematic errors due to the analysis process. According to equation 5, a SHT at 510 °C for 10 min could lead to the maximum improvement of YS of 20 MPa, compared with SHTB.

Table 8. Inter-particle spacing ( $\lambda$ ) and increased strength due to the Orowan mechanism for different SHT conditions.

Temperature ( $T_{\text{SHT}}$ )	Soaking time ( $t_{\text{SHT}}$ )	$\lambda$ [ $\mu\text{m}$ ]	$\Delta\sigma_{th}$ [Mpa]	$\Delta\sigma_{th} - \Delta\sigma_{540^\circ\text{C}-1h}$ [Mpa]
450 °C	1h	$0.78 \pm 0.01$	$30 \pm 0.2$	9
	2h	$0.93 \pm 0.02$	$25 \pm 0.4$	4
	5min	$0.59 \pm 0.02$	$39 \pm 1.6$	18
510 °C	10min	$0.57 \pm 0.02$	$41 \pm 1.3$	20
	15min	$0.60 \pm 0.01$	$39 \pm 0.8$	18

540 °C	20min	$0.67 \pm 0.02$	$35 \pm 0.8$	14
	30min	$0.81 \pm 0.04$	$29 \pm 1.5$	8
	1h	$0.86 \pm 0.01$	$27 \pm 0.4$	6
	1h	$1.11 \pm 0.06$	$21 \pm 1.1$	x

Several authors [35,37,39] have reported a positive effect on the mechanical performance of the LPBF AlSi10Mg of a homogeneous distribution of small Si particles in the  $\alpha$ -Al matrix. Moreover, a finer microstructure can lead to a further improvement in the mechanical performance of the alloy, since small Si particle size means high cohesion of the particles with the  $\alpha$ -Al matrix and hence higher alloy strength and ductility. However, to the best of the authors' knowledge, a quantitative evaluation of their effects was yet to be carried out.

The size distribution of the Si particles for the samples which underwent SHTR and SHTB is reported in Figure 10. These results point out the difference between the area of the Si particles in the SHTR compared with the SHTB samples. For the first one, about 98% of the Si particles is characterized by an area below  $0.5 \mu\text{m}^2$ , while for the latter the Si particle area distribution is shifted up to  $5 \mu\text{m}^2$  (Fig. 10).

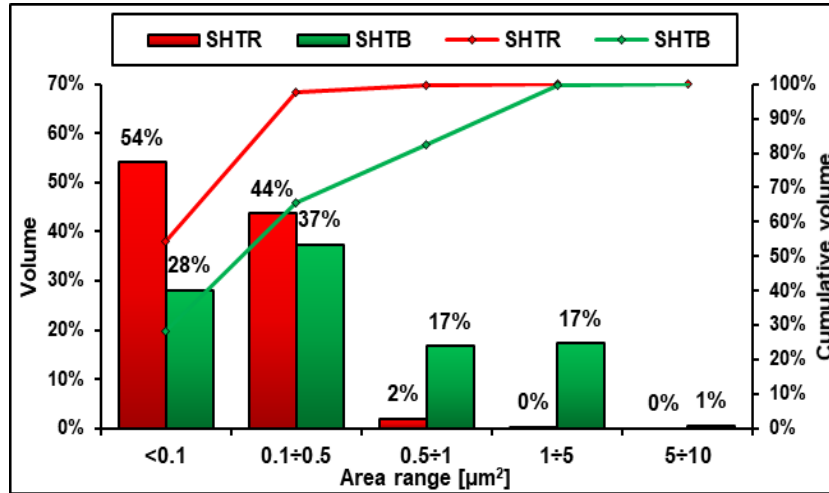


Fig. 10. Area distribution of Si particles for SHTR ( $T_{\text{SHT}}=510 \text{ }^{\circ}\text{C}$  and  $t_{\text{SHT}}=10 \text{ min}$ ) and SHTB ( $T_{\text{SHT}}=540 \text{ }^{\circ}\text{C}$  and  $t_{\text{SHT}}=1 \text{ h}$ ) conditions.

From the results of density measurements, XRD and microstructural analyses, SHTR offers several advantages by comparison with the other SHT conditions in that: (i) it limits the increase in the porosity content due to high temperature exposure; (ii) it leads to finer and more homogeneous microstructure in terms of eutectic Si particles; (iii) it favors the development of a more supersaturated  $\alpha$ -Al matrix; (iv) it should induce both higher strength and ductility after subsequent aging. Therefore, the SHTR has been identified as the optimal SHT for the LPBF AlSi10Mg alloy.

### 3.4 Aging curves

The effect of artificial aging on the hardness of the LPBF AlSi10Mg alloy has been studied in both the AB and SHTR conditions to evaluate the aging curves for T5 and T6R heat treatments.

The aging curves on AB samples at  $160 \text{ }^{\circ}\text{C}$ ,  $170 \text{ }^{\circ}\text{C}$  and  $180 \text{ }^{\circ}\text{C}$  for times up to 8 h are reported in Figure 11.a. The curves highlight that after AA the hardness decreases compared with the hardness of the AB alloy. The reduction is negligible up to 4 h at  $160 \text{ }^{\circ}\text{C}$ , while for the other temperatures the decrease in hardness was already observed after 1 h. At  $160 \text{ }^{\circ}\text{C}$  and  $170 \text{ }^{\circ}\text{C}$  the maximum hardness drop is respectively 4% and 6% after 8 h, while at  $180 \text{ }^{\circ}\text{C}$  a significant hardness drop of about 15% already occurs after 5 h. This

behavior can be explained considering that the manufacturing process of the samples is carried out using a heated platform (150 °C) and takes about 30 h. This promotes the formation of strengthening acicular nano-sized Si precipitates within the cells of the  $\alpha$ -Al matrix, as observed in Figure 11.a. AA, as a function of the aging temperature and time, may not have appreciable effects on Si precipitates or it may induce their coarsening with a consequent decrease of the material hardness at temperatures higher than 150 °C.

The aging curves (Fig. 11.b) of the alloy after SHTR (T6R heat treatment) show the typical trend for solution treated and quenched Al alloys, where hardness increases with increasing aging time and the peak aging condition shifts to shorter aging times with increasing aging temperature. It is worth noting that the SHTR, because of its effects on the microstructure (described in section 3.3), causes a hardness drop of about 45% compared to the AB condition. This drop is only partially recovered after the aging treatment because of the precipitation of  $\beta''$  and  $\beta'$  strengthening phases [5,31,45].

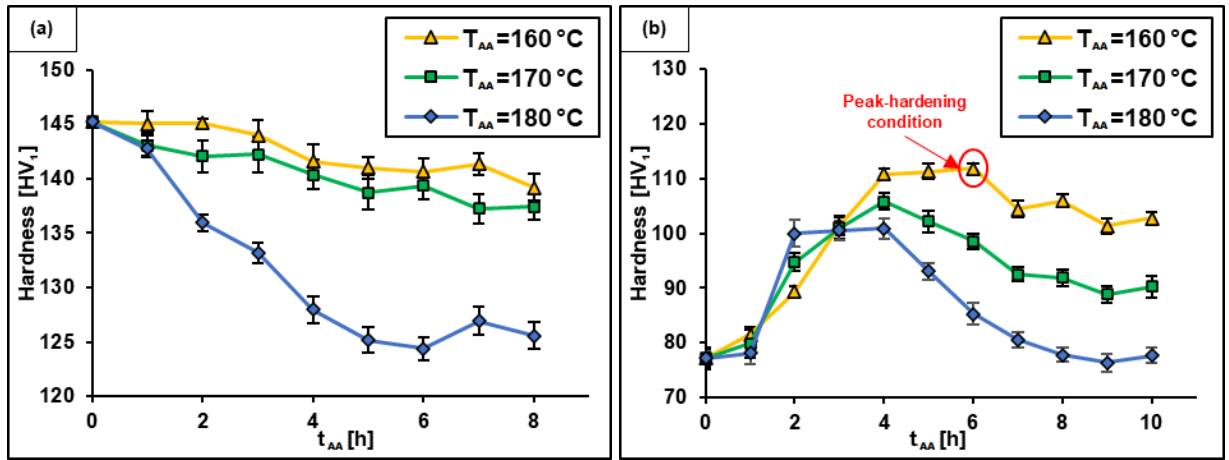


Fig. 11. Aging curves related to the conditions: (a) AB, (b) SHTR LPBF AlSi10Mg alloy at 160 °C, 170 °C, 180 °C.

As a matter of fact, even in the peak-aged condition ( $T_{AA}=160$  °C and  $t_{AA}=6$  h) the hardness drop is equal to 23% compared with the AB alloy. Despite the hardness reduction these data agree with data already published [5,15,37,38] for T6 heat-treated LPBF AlSi10Mg alloy, further confirming the effectiveness of the SHTR compared with a conventional SHT. Similar trends of the aging curves have identified by different authors [31,37,45], even if peak-hardening conditions have been identified for a longer time. Zhou et al. [45], starting from conventional T6 solution treatment conditions ( $T_{SHT}=520$  °C and  $t_{SHT}=2$  h and  $T_{AA}=160$  °C), identified the peak-hardening condition at 10 h. Comparable results were obtained by Padovano et al. [31] in the same T6 heat treatment conditions. However, the aging curves in the present paper show that the peak-hardening conditions moves towards shorter aging time, occurring after 6 h. Probably this behavior is due to the higher Si supersaturation induced by SHTR compared to conventional SHT, which accelerates the precipitation kinetics hardening after quenching [60]. This finding agrees also with Wang et al. [6] and Zhou et al. [45], who highlighted that in LPBF AlSi10Mg alloy the precipitation kinetics and the results of T6 are closely linked to the effectiveness of the SHT.

The aging curves at 170 °C and 180 °C, compared with the curve at 160 °C, show: (i) a shift of the peak hardness to a shorter  $t_{AA}$  (3 h instead of 6 h); (ii) a lower peak hardness (7 and 11%, respectively); (iii) a faster overaging, with a residual hardness after 8 h at 180 °C equal to the hardness of the alloy after SHTR. In addition, for these aging temperatures the hardness trends agree with those reported in the literature [31,38,45], but with the peak hardness shifted to shorter  $t_{AA}$  because of the faster precipitation kinetics. It is



moreover worth nothing that after 8 h at 180 °C the residual hardness is the same as the SHTRed alloy [15,61].

In the light of the above, the influence of the following heat treatment conditions on the tensile behavior of LPBF AlSi10Mg alloy was assessed and compared with the T6B:

- (i) T5 direct artificial aging: 160 °C for 4 h and air cooling, with the aim of slightly increasing the elongation to failure of the alloy compared with AB alloy.
- (ii) T6 rapid solution treatment (T6R): SHTR at 510 °C for 10 min, water quenching at room temperature, artificial aging at 160 °C for 6 h and air cooling, to test the peak-hardening condition.

### 3.5 Tensile Tests

The tensile behavior and hardness values of the LPBF AlSi10Mg alloy after the T5 and T6R heat treatments were compared with those of the LPBF AlSi10Mg alloy in the AB and T6B conditions. The hardness  $HV_1$  of the tensile samples and the results of the tests are reported in Figure 12, while representative stress-strain curves are reported in Figure 13.

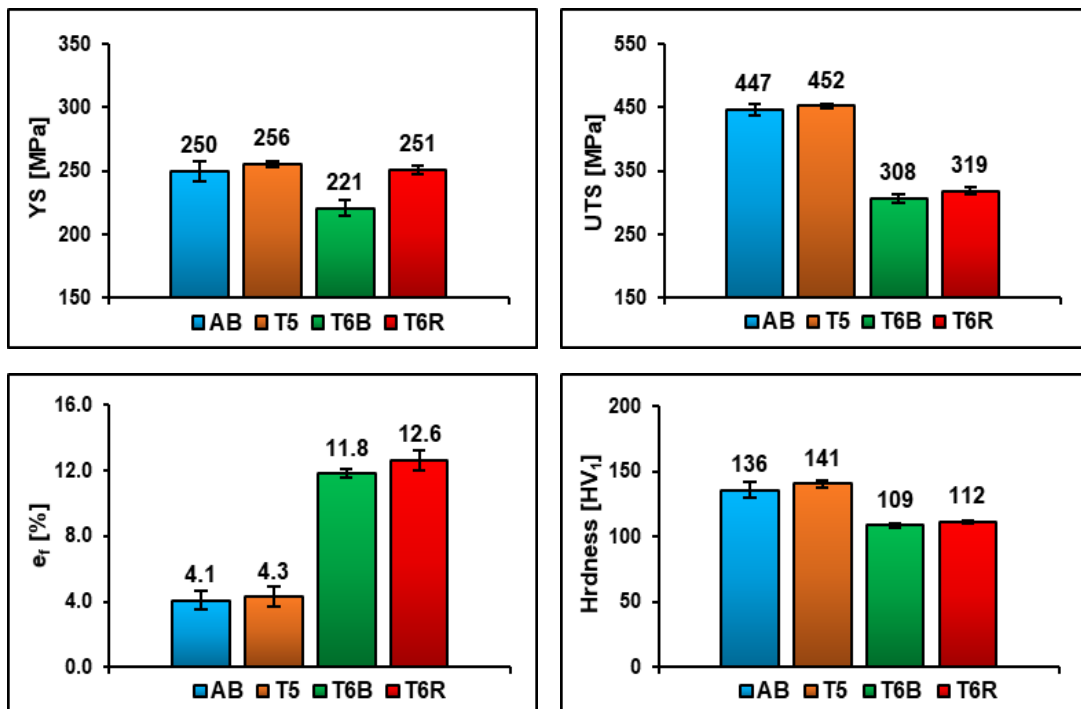


**Fig. 12.** Tensile properties and hardness of the LPBF AlSi10Mg alloy related to the conditions: (i) AB, (ii) T5 (AA at 160 °C for 4 h), (iii) T6B (SHTB at 540 °C for 1 h and AA at 160 °C for 4 h) and (iv) T6R (SHTR at 510 °C for 10min and AA at 160 °C for 6 h).

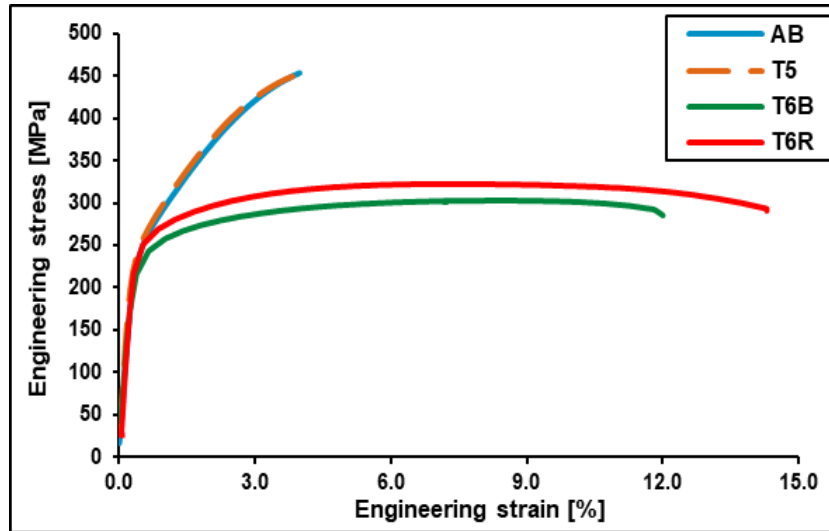


**Fig. 13** Representative tensile stress-strain curves of the LPBF AlSi10Mg alloy related to the conditions: (i) AB, (ii) T5 (AA at 160 °C for 4 h), (iii) T6B (SHTB at 540 °C for 1 h and AA at 160 °C for 4 h) and (iv) T6R (SHTR at 510 °C for 10min and AA at 160 °C for 6 h).

Among the tested samples, the AB and T5 heat-treated samples show the highest strength, as well as the lowest elongation to failure (Fig. 12), due to the concurrent effect of several strengthening mechanisms typical of their peculiar microstructure: microstructural refinement, solid solution, aggregated second phase (eutectic Si network), high dislocation density and precipitation hardening.

The T5 heat treatment leads to a slight increase of the tensile properties compared with the AB condition, respectively equal to 3.7% for hardness, 1.1% and 2.4% for UTS and YS, and 4.8% for  $\epsilon_f$ . According to the literature survey [15,24,25] this slight improvement of the mechanical performance of the T5 heat-treated alloy could be related to: (i) the formation of acicular nano-sized Si precipitates within the cells of the Al matrix, (ii) the partial stress relief occurring during the T5 heat treatment and (iii) the preservation of the AB microstructure with its main strengthening mechanisms. The higher improvement of the mechanical performance reported in the literature by the T5 heat treatment [15,25] than that recorded in the present work is attributable to the use of a not heated platform in these studies, while in the present work the platform was heated to 150 °C. Platform heating, in fact, increases the amount of acicular nano-sized Si strengthening precipitates that already form during the building of the samples in the cells of the  $\alpha$ -Al matrix, as confirmed by the previously reported microstructural analyses (Fig. 8.a and 8.b). Therefore, it can be inferred that the T5 heat treatment performed in the present study had a lower effect on the amount of Si precipitates and, consequently, on their strength by comparison to [15,25], due to the heated platform. The T5 heat treatment, moreover, had no beneficial effects on the ductility due to its negligible effect on the MPB, which ensures a preferential path for the crack growth during the tensile tests analogous to that observed in the AB samples (see section 3.6.1).

On the contrary, the T6B induces a YS reduction of about 10%, a UTS reduction of about 45% but an increase of the  $\epsilon_f$  of about 200% compared to both the AB and the T5 heat-treated alloy.

These findings agree with the results reported in [5,15,25,35,37] and have been widely explained in the light of the microstructural changes which take place mainly during the SHT, such as the disappearance of the MP structure or the development of the composite-like microstructure of Si particles in  $\alpha$ -Al phase matrix in place of the cellular structure [15,22,32,33]. These microstructural changes, in fact, induce a remarkable reduction of the solid solution reinforcement, the loss of both microstructural refinement and aggregate

second phase strengthening mechanisms, and a drop in the dislocation density. The loss of the main strengthening mechanisms active in the AB alloy is only partially balanced by the precipitation of both  $\beta''$  and  $\beta'$  strengthening phases and the dispersed second phase reinforcement, due to the presence of globular Si particles inside the  $\alpha$ -Al matrix. In contrast, the disappearance of scan tracks, MPB and HAZ, besides an overall reduction of the inhomogeneity inside the microstructure and of the internal residual stresses, leads to an increase of the ductility of the alloy.

The new proposed T6R heat treatment induces an increase of both strength (about 14% and 4% for YS and UTS, respectively) and ductility (about 7% for  $e_f$ ) compared with the T6B heat treatment, while comparison with AB and T5 samples shows similar YS and significantly higher elongation to failure (more than 200%), while UTS is lower at about 30%.

The increase in mechanical performance both in terms of strength and ductility of the T6R compared to the T6B treatment can be mainly ascribed to its finer and more homogeneous microstructure (widely described in section 3.3). The smaller Si particles, in fact, allow: (i) an increase in the effect of the Orowan strengthening mechanism; (ii) an increase in the cohesion between Si particles and  $\alpha$ -Al matrix; (iii) a reduction in the tendency of the Si particles to fracture; (iv) a reduction in the gas porosity content [25,35,37,39].

These considerations are confirmed by the fact that equation 5, which estimates the increase of the alloy strength due to the Orowan mechanism, was able to evaluate with good approximation the effect on the YS of the alloy of the different composite-like microstructures induced by T6R and T6B. According to equation 5, the T6R samples have a higher YS of 20 MPa compared to T6B ones, a value in agreement with the results of the tensile tests that highlighted a difference ( $\Delta YS$ ) between the YS of the T6R and T6B samples of 30 MPa. This small difference between calculated and measured  $\Delta YS$  could be ascribed to the effects of the other microstructural changes on the above reported strengthening or failure mechanisms.

It is finally worth noting how the microstructure also affects the strain-hardening capability of the LPBF AlSi10Mg alloy. The AB and T5 alloys, as highlighted by the stress-strain curves (Fig. 13), show a higher strain hardening compared to that of the T6R and T6B samples. According to Chen et al. [21] this behavior is mainly due to the ultrafine cellular structure and indicates the possibility for ultrafine cellular structures, obtained by means of LPBF, to achieve large uniform elongations. The presence of an inhomogeneous microstructure, with MPB, HAZ and defects such as pores and lack of fusion, however, reduces the elongation to failure of the AB and T5 samples, so that it is lower than the uniform deformation of T6B and T6R samples which have a coarser but more homogeneous microstructure.

### 3.6 Fractography

With the aim of highlighting the effect of heat treatment conditions on the fracture mechanisms of LPBF AlSi10Mg alloy, the analysis of the fracture surfaces was carried out both by OM and by SEM to identify the main failure mechanisms.

#### 3.6.1 OM Analyses

In the AB and T5 heat-treated alloy (Fig. 14), the fracture propagates preferentially along the MPB. These regions are characterized by a coarser microstructure, lower Si content (for the larger  $\alpha$ -Al cells area) and

higher density of defects (like lack of fusions), representing the weakest zones of the microstructure [16]. No significant differences in the macro and micro fracture features have been observed between T5 and AB samples, further confirming that the direct aging treatment after the LPBF process has no substantial effects on the alloy microstructure.

In contrast, in both T6B and T6R heat-treated alloys (Fig. 15) the fracture propagates joining the pores present at the Si particles/ $\alpha$ -Al matrix interface, originated by the decohesion of the Si particles from the matrix [12]. The fracture mechanism is like cast Al-Si alloys, where the nucleation of the micro-voids occurs at the soft matrix/hard phase interface, followed by growth and coalescence of the voids. However, because of the finer and more homogeneous Si particle distribution, it is possible to observe a smoother crack path in the failed T6R compared to the T6B samples (Fig. 15). As a matter of fact, the larger and more irregular Si particles and the higher amount of gas porosities in the T6B compared to the T6R samples induce the formation of larger pores (Fig. 15), which promote failure under tensile loading with the development of rougher fracture surfaces.

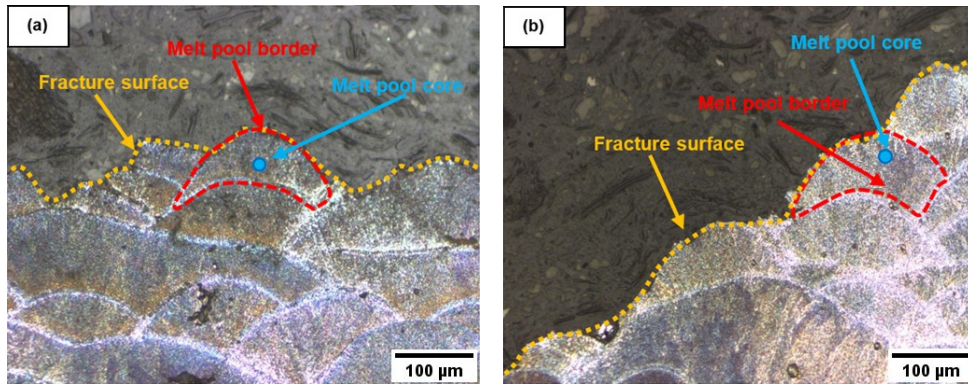


**Fig. 14.** Longitudinal section of the fracture surface relative to the (a) AB and (b) T5 conditions. Each optical micrograph shows the same crack propagation path along the MPB.

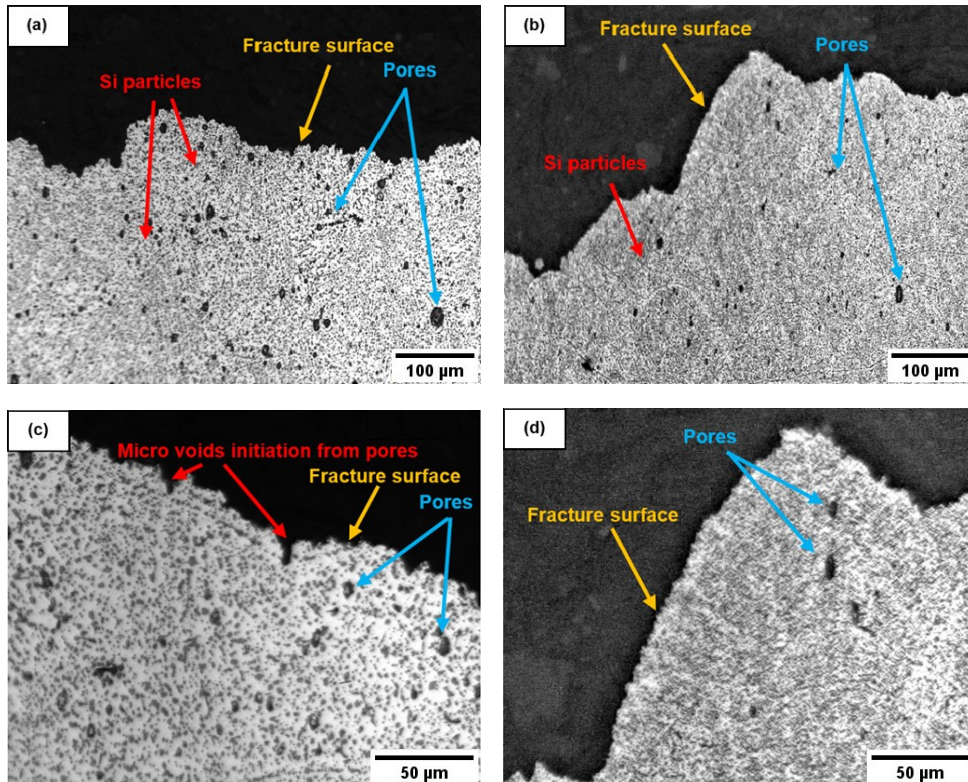


**Fig. 15.** Longitudinal section of the fracture surface relative to the (a,c) T6B and (b,d) T6R conditions. The T6B samples show larger Si particles, higher internal pore density and higher fracture surface roughness than the T6R samples.

### 3.6.2 SEM Analyses

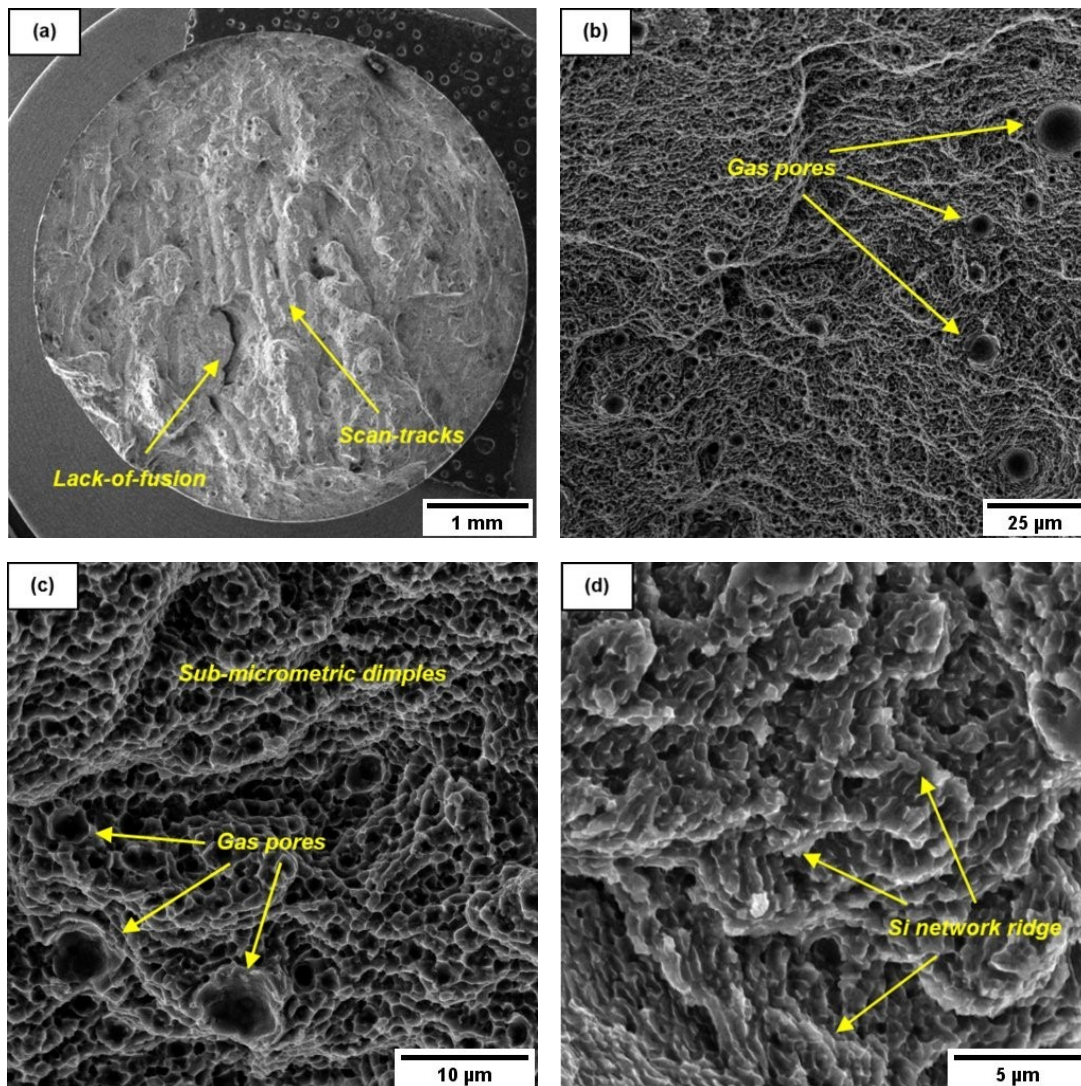
As described in the previous section, AB and T5 heat-treated LPBF AlSi10Mg samples show the same fracture surface morphologies. Focusing on the AB condition, the low magnification SEM images of the fracture surfaces (Fig. 16.a and 16.b) highlight: (i) an interlayer fracture path, (ii) large defects (lack of fusion and pores), (iii) flat zones where scan-track segments are clearly visible and (iv) a crack path that develops due to decohesion at the interface between the Si eutectic network and the  $\alpha$ -Al matrix [32]. These images agree with the previous observations, highlighting the development of the fracture path mainly through the weakest zones of the microstructure such as MPB, HAZ and defects. This preferential fracture path induces an inter-layer fracture with consequent low  $\epsilon_f$ . Fracture surfaces at higher magnification (Fig. 16.c, 16.d) are characterized by shallow micro and sub-micrometric dimples, with a jagged, sharp, and irregular morphology. This morphology is probably due to the tear-fracture mechanism at the Si network/ $\alpha$ -Al cells interface, which leads to the formation of dimples with a size and morphology that mirrors the sub-cellular microstructure of the alloy and reflects the high strength and low ductility of the material. This feature is probably accentuated by the presence of Si nanoparticles within the center of the cellular eutectic cells (highlighted in section 3.3), which further increase the strength of  $\alpha$ -Al and reduce its ductility [27,30].

The microstructure evolution induced by T6 heat treatments also significantly modified the fracture morphology of both T6B and T6R samples compared with AB and T5 samples, mainly at high magnification.

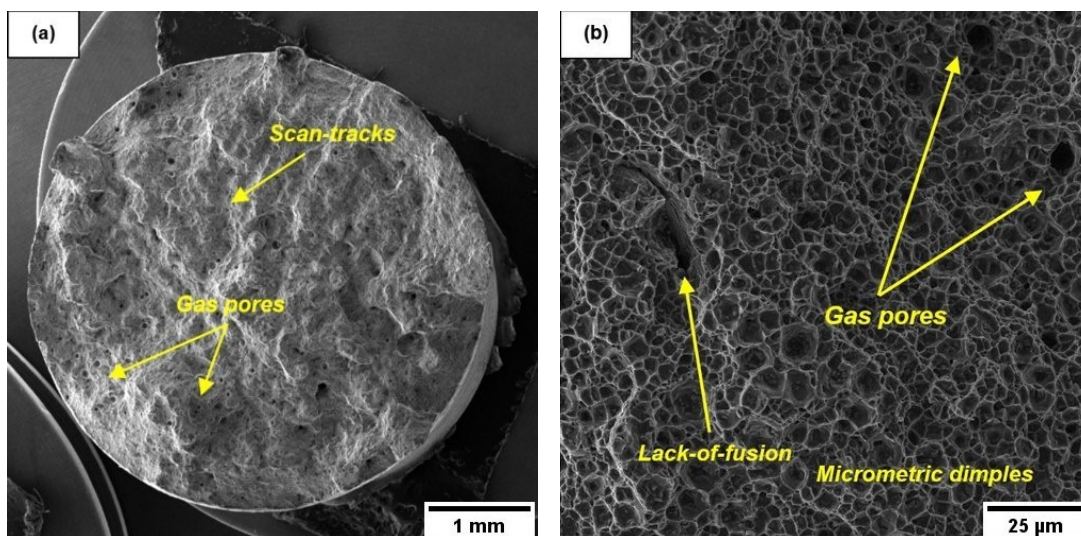
At low magnification (Fig. 17.a, 17.b, 18.a and 18.b) fracture surfaces of both T6B and T6R are characterized by irregular surfaces and large defects, mainly pores. Even if the T6 heat treatments actually homogenize the microstructure and delete the MPB and HAZ [5,36,39], which represent a preferential crack path, some scan tracks are still observed, in agreement with the findings of Girelli et al. [62]. The fracture surface analyses, in contrast, are not able to highlight a clear increase in gas porosity in the T6 heat-treated alloy compared with AB or T5 heat-treated samples, as pointed out by the density measurements (section 3.1). The differences in both the amount and size of gas pores appears negligible among the AB, T5, T6R and T6B samples and this can be explained considering that, independently from the samples condition, the crack propagates through the weakest path with the highest number of defects.

Fracture surface analyses at high magnification of both T6B and T6R samples show a completely ductile failure mode, characterized by deep dimples (Fig. 17.c and 18.c), instead of the shallow dimples observed in the AB and T5 samples. However, the different size and distribution of the Si particles in the alloy after T6B and T6R heat treatment clearly affect the dimples feature, despite the same fracture mechanism. In the T6B samples, the coarse and inhomogeneously distributed Si particles lead to the formation of large and very deep dimples and tear ridges (Fig. 17.d). The first are caused by the decohesion between Si particles and Al matrix or the fracture of the larger Si particles [27,32,63], while the latter is caused by local plastic flow induced by the presence of large particles or pores close to each other. In the T6R samples, in comparison, the Si particles are less prone to fracture because of their smaller size and globular morphology, and therefore the dimples mainly nucleate at the Si particle/ $\alpha$ -Al matrix interface rather than by cracked particles (Fig. 18.d). The homogeneous distribution of the fine Si particles induces the development of finer dimples and a more uniform plastic deformation, compared to the T6B alloy.





**Fig. 16.** FEG-SEM images of the fracture surfaces of the LPBF AlSi10Mg parts in AB condition at different magnifications: (a) 40x, (b) 1.50kx, (c) 5.00kx, (d) 10.00kx.





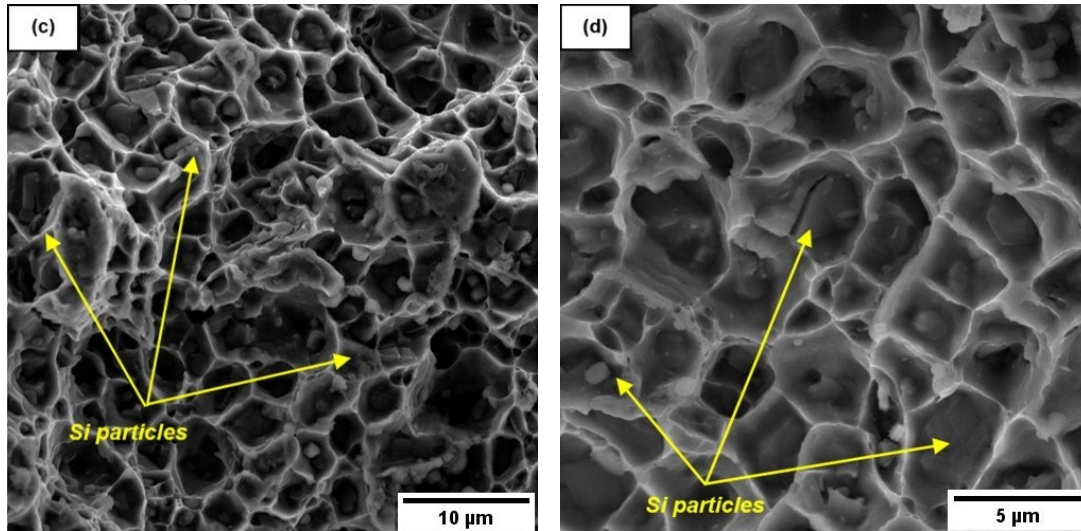


**Fig. 17.** FEG-SEM images of the fracture surfaces of the LPBF AlSi10Mg parts in T6B condition at different magnifications: (a) 40x, (b) 1.50kx, (c) 5.00kx, (d) 10.00kx.

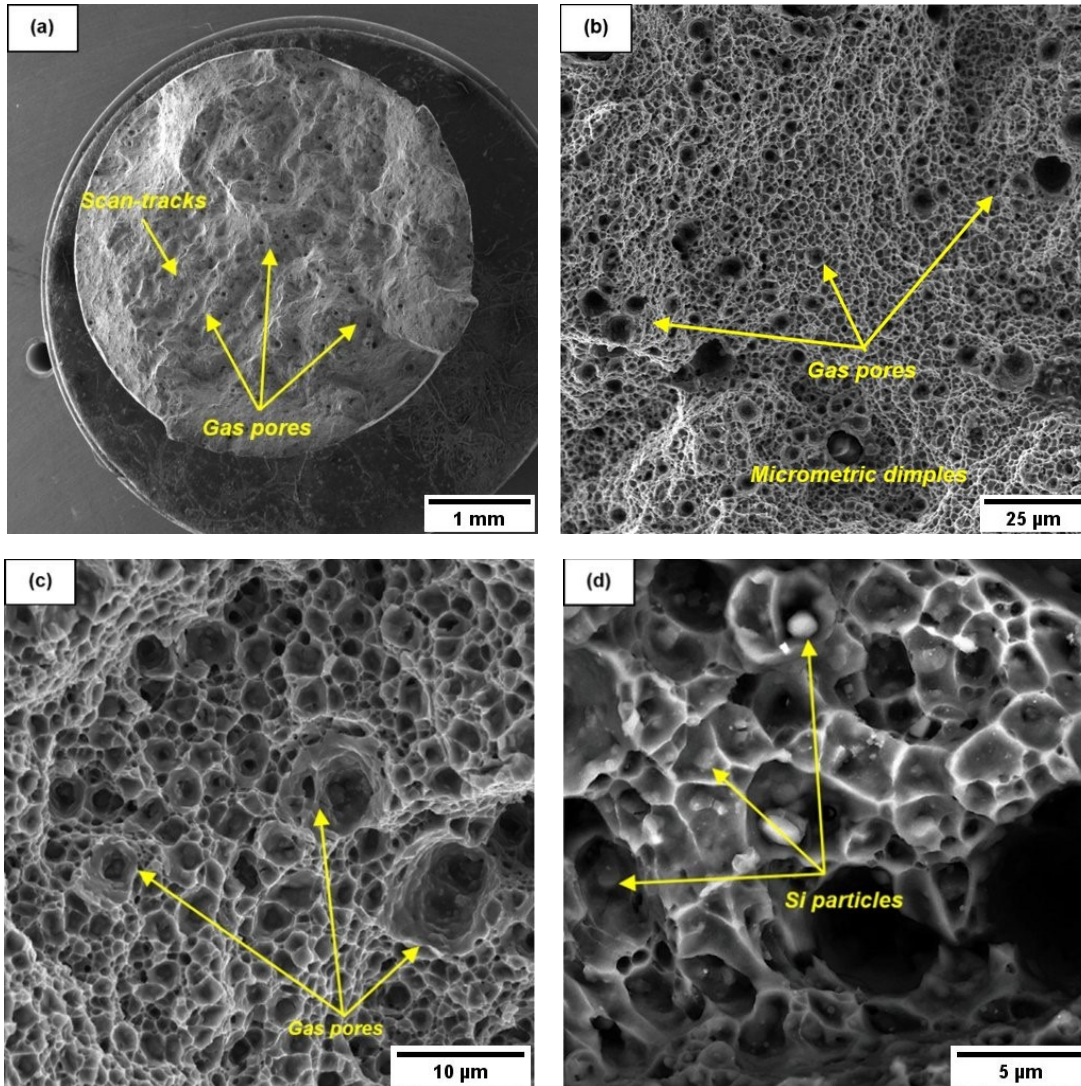


**Fig. 18.** FEG-SEM images of the fracture surfaces of the LPBF AlSi10Mg parts in T6R condition at different magnifications: (a) 40x, (b) 1.50kx, (c) 5.00kx, (d) 10.00kx.

## 6 Conclusions

In the present work the effects of a different SHT and AA condition on the microstructure of the LPBF AlSi10Mg alloy were investigated. This study allowed the definition of a customized heat treatment (T6R) for the LPBF AlSi10Mg alloy, consisting of a rapid SHT (510 °C for 10 min) followed by AA (160 °C for 6 h). The performance of the T6R heat-treated LPBF AlSi10Mg alloy was compared with the alloy subjected to different heat treatment conditions: AB, T5 heat-treated (direct AA of the AB alloy for at 160 °C for 4 h) and conventionally T6 heat-treated (T6B) consisting of a SHT (540 °C for 1 h) followed by AA (160 °C for 4 h). The T6B was considered the benchmark condition.

The following conclusions can be drawn:

- The SHT increases the volume of the gas pores in the LPBF AlSi10Mg alloy. The use of low temperatures and/or short times limits their expansion.
- The SHTR (510 °C and time between 5 and 20 min) allows a higher level of Si supersaturation in the  $\alpha$ -Al matrix in comparison to both the AB alloy and the alloy subjected to longer soaking time.
- The SHTR leads to the development of a composite-like microstructure of Si particles embedded in the  $\alpha$ -Al phase matrix. Compared with the Si particles induced by conventional SHT, these are finer and more homogeneous both in size and distribution.
- The SHTR accelerates the kinetics of precipitation hardening, moving the peak-hardening condition towards a shorter time.
- The T6R improves YS, UTS and  $e_f$  by about 14%, 4% and 7% respectively, compared with the T6B heat treatment. Moreover, the T6R AlSi10Mg alloy, compared to the AB and T5 alloy, has a similar YS and a higher elongation (about 210%), but lower UTS (about 30%).
- The estimation of the Orowan strengthening effect, due to the Si particles present in the T6R and T6B heat-treated alloy, confirms that the static mechanical properties of the LPBF AlSi10Mg alloy are affected more by the size and distribution of the Si particles than by other microstructural features.
- The AB and T5 heat-treated alloy present similar fracture paths, preferentially along the MPB. However, because of the absence of the MPB after T6 heat treatment, in the T6 heat-treated alloy the failure propagation occurs linking both the voids formed at the Si particles/ $\alpha$ -Al matrix interface and the inner pores. Moreover, at high magnification the fracture surfaces show shallow dimples in the AB and T5 heat-treated alloy and deep dimples in the T6 heat-treated alloy. The latter are finer in the samples that have undergone T6R compared to those that underwent T6B.

After the investigations reported in this work, some issues remain still open:

- The effect of the T6R on residual stresses, epitaxial grains and therefore on the fatigue behavior of the material;
- The influence of the starting microstructure of LPBF AlSi10Mg (generated by LPBF process parameters used for the production of the AlSi10Mg samples) on the optimal parameters of the T6R heat treatment.

These issues will be investigated in the next steps of this research.



## Acknowledgments and Funding Information

The present work was supported by the RIMMEL project, CUP B91F18000370009, POR FESR EMILIA ROMAGNA 2014-2020, Asse 1 - Ricerca e Innovazione.

The authors declare that they have no conflict of interest.

We wish to thank Dr. Ramona Sola at the CIRI MAM (University of Bologna) for XRD analyses.

## References

1. T. DebRoy, H.L. Wei, J.S. Zuback, T. Mukherjee, J.W. Elmer, J.O. Milewski, A.M. Beese, A. Wilson-Heid, A. De, W. Zhang, *Progress in Materials Science*, 2018, Volume 92, Pages 112-224.
2. Trevisan, F.; Calignano, F.; Lorusso, M.; Pakkanen, J.; Aversa, A.; Ambrosio, E.P.; Lombardi, M.; Fino, P.; Manfredi, D., *Materials* 2017, no. 1: 76.
3. N. T. Aboulkhair, M. Simonelli, L. Parry, I. Ashcroft, C. Tuck, R. Hague, 2019, Volume 106, p.100578.
4. U. Tradowsky, J. White, R.M. Ward, N. Read, W. Reimers, M.M. Attallah, *Materials & Design*, 2016, Volume 105, Pages 212-222.
5. N. T. Aboulkhair, I. Maskery, C. Tuck, I. Ashcroft, N. M. Everitt, *Materials Science and Engineering: A*, 2016, Volume 667, Pages 139-146.
6. L.F. Wang, J. Sun, X.L. Yu, Y. Shi, X.G. Zhu, L.Y. Cheng, H.H. Liang, B. Yan, L.J. Guo, *Materials Science and Engineering: A*, 2018, Volume 734, Pages 299-310.
7. D. Buchbinder, H. Schleifenbaum, S. Heidrich, W. Meiners, J. Bültmann, *Physics Procedia*, 2011, Volume 12, Part A, Pages 271-278.
8. E.O. Olakanmi, R.F. Cochrane, K.W. Dalgarno, *Progress in Materials Science*, 2015, Volume 74, Pages 401-477.
9. J. Zhang, B. Song, Q. Wei, D. Bourell, Y. Shi, *Journal of Materials Science & Technology*, 2019, Volume 35, Issue 2, Pages 270-284.
10. L. Thijs, K. Kempen, J. Kruth, J. V. Humbeeck, *Acta Materialia*, 2013, Volume 61, Issue 5, Pages 1809-1819.
11. X. Liu, C. Zhao, X. Zhou, Z. Shen, W. Liu, *Materials & Design*, Volume 168, 2019, 107677.
12. N. Read, W. Wang, K. Essa, M. M. Attallah, *Materials & Design (1980-2015)*, 2015, Volume 65, Pages 417-424.
13. J. Wu, X.Q. Wang, W. Wang, M.M. Attallah, M.H. Loretto, *Acta Materialia*, 2016, Volume 117, Pages 311-320.
14. A. Hadadzadeh, B. S. Amirkhiz, M. Mohammadi, *Materials Science and Engineering: A*, 2019, Volume 739, Pages 295-300.
15. M. Fousová, D. Dvorský, A. Michalcová, D. Vojtěch, *Characterization*, 2018, Volume 137, Pages 119-126.
16. Z.H. Xiong, S.L. Liu, S.F. Li, Y. Shi, Y.F. Yang, R.D.K. Misra, *Materials Science and Engineering: A*, 2019, Volumes 740-741, Pages 148-156.
17. P. Wei, Z. Wei, Z. Chen, J. Du, Y. He, J. Li, Ya. Zhou, *Applied Surface Science*, 2017, Volume 408, Pages 38-50.
18. Tang, M., Pistorius, P.C., *JOM* 69, 2017, 516-522.
19. C. Galy, E. Le Guen, E. Lacoste, C. Arvieu, *Additive Manufacturing*, 2018, Volume 22, Pages 165-175.
20. Tonelli L, Liverani E, Valli G, Fortunato A, Ceschini L., *Int J Adv Manuf Technol*, 2020, 106, 371-383.
21. B. Chen, S.K. Moon, X. Yao, G. Bi, J. Shen, J. Umeda, K. Kondoh, *Scripta Materialia*, 2017, Volume 141, Pages 45-49.
22. J. Fite, S. E. Prameela, J. A. Slotwinski, T. P. Weihs, *Additive Manufacturing*, 2020, Volume 36, 101429.
23. K.G. Prashanth, J. Eckert, *Journal of Alloys and Compounds*, 2017, Volume 707, Pages 27-34.
24. Fiocchi, J., Biffi, C.A., Colombo, C., L. M. Vergani & A. Tuissi, *JOM* 72, 2020, 1118-1127.
25. Casati, R. & Hamidi & Coduri, M. & Tirelli, V. & Vedani, M, *Metals* 2018, 8, 954.
26. Tonelli, L., Liverani, E., Morri A. & Ceschini L., *Metall Mater Trans B*, 2021, 52, 2484-2496.
27. I. Rosenthal, R. Shneck, A. Stern, *Materials Science and Engineering: A*, 2018, Volume 729, Pages 310-322.
28. N. E. Uzan, R. Shneck, O. Yeheskel, N. Frage, *Materials Science and Engineering: A*, 2017, Volume 704, Pages 229-237.
29. Mfusi, B & Mathe, Ntombizodwa & Popoola, P & Tshabalala, L., *IOP Conference Series: Materials Science and Engineering*. 2019. 655. 012027.
30. N. Takata, H. Kodaira, K. Sekizawa, A. Suzuki, M. Kobashi, *Materials Science and Engineering: A*, 2017, Volume 704, Pages 218-228.
31. E. Padovano, C. Badini, A. Pantarelli, F. Gili, F. D'Aiuto, *Journal of Alloys and Compounds*, 2020, Volume 831, 154822.
32. W. Li, S. Li, J. Liu, A. Zhang, Y. Zhou, Q. Wei, C. Yan, Y. Shi, *Materials Science and Engineering: A*, 2016, Volume 663, Pages 116-125.
33. Julius N. Domfang Ngnekou, Y. Nadot, G. Henaff, J. Nicolai, W. H. Kan, J. M. Cairney, L. Ridosz, *International Journal of Fatigue*, 2019, Volume 119, Pages 160-172.
34. F. Alghamdi, X. Song, A. Hadadzadeh, B. Shalchi-Amirkhiz, M. Mohammadi, M. Haghshenas, *Materials Science and Engineering: A*, 2020, Volume 783, 139296.
35. Iturrioz, A., Gil, E., Petite, M.M., F. Garciandia, A. M. Mancisidor & M. San Sebastian. *Weld World* 62, 2018, 885-892.
36. W. H. Kan, Y. Nadot, M. Foley, L. Ridosz, G. Proust, J. M. Cairney, *Additive Manufacturing*, 2019, Volume 29, 100805.
37. Tocci, M., Pola, A., Gelfi, M., Marcello Gelfi & Giovina Marina La Vecchia *Metall Mater Trans A*, 2020, 51, 4799-4811.
38. Mertens, A.; Dedry, O.; Reuter, D.; Rigo, O.; Lecomte-Beckers, J., In *Proceedings of the 26th International Solid Freeform Fabrication Symposium*, Dayton, OH, USA, 23-26 June 2015, pp. 1007-1016.
39. C. Zhang, H. Zhu, H. Liao, Y. Cheng, Z. Hu, X. Zeng, *International Journal of Fatigue*, 2018, Volume 116, Pages 513-522.
40. Li, C.; Liu, Z.Y.; Fang, X.Y.; Guo, Y.B.. *Procedia CIRP*. 2018, 71, 348-353
41. SLM Solution Group AG, DE, [Online]. Available: <https://www.slm-solutions.com/it/prodotti/machines/slmr500/>
42. International Organization for Standardization: ISO 14707:2015: Surface chemical analysis— Glow discharge optical emission spectrometry (GD-OES) — Introduction to use; International Organization for Standardization: Geneva, Switzerland, 2015.
43. Lumley, R., O'Donnell, R., D.R. Gunasegaram & M. Givord, *Metall and Mat Trans A*, 2007, 38, 2564-2574.
44. Lumley, R.N., Polmear, I.J. & Curtis, P.R., *Metall and Mat Trans A*, 2009, 40, 1716-1726.
45. L. Zhou, A. Mehta, E. Schulz, B. McWilliams, K. Cho, Y. Sohn, *Materials Characterization*, 2018, Volume 143, Pages 5-17.
46. ASM International. ASTM B962-17: Standard Test Methods for Density of Compacted or Sintered Powder Metallurgy (PM) Products Using Archimedes' Principle, ASM International: West Conshohocken, PA, USA, 2017.
47. K.H. Eckelmeyer, *X-Ray Diffraction for Bulk Structural Analysis*, Metals Handbook Desk Edition, Second Edition, 1998.
48. G. Poli, R. Sola, P. Veronesi, *Materials Science and Engineering A*, 2006, 441, 149-156.

49. ASM International. ASTM E3-11(2017): Standard Guide for Preparation of Metallographic Specimens, ASM International: West Conshohocken, PA, USA, 2017.
50. ASM International. ASTM E407-07(2015): Standard Practice for Microetching Metals and Alloys, ASM International: West Conshohocken, PA, USA, 2015.
51. M Li, S Ghosh, O Richmond, H Weiland, T.N Rouns, Materials Science and Engineering: A, 1999, Volume 265, Issues 1–2, Pages 153-173.
52. ASM International. ASTM E92-17: Standard Test Methods for Vickers Hardness and Knoop Hardness of Metallic Materials, ASM International: West Conshohocken, PA, USA, 2017.
53. International Organization for Standardization. ISO 6892-1:2009, Metallic Materials–Tensile Testing–Part 1: Method of Test at Room Temperature; International Organization for Standardization: Geneva, Switzerland, 2009.
54. International Organization for Standardization. ISO 6892-2:2011, Metallic Materials–Tensile Testing–Part 2: Method of Test at Elevated Temperature; International Organization for Standardization: Geneva, Switzerland, 2011.
55. A. Bendijk, R. Delhez, L. Katgerman, T.H. De Keijser, E.J. Mittemeijer, N.M. Van Der Pers, J Mater Sci, 1980, 15, 2803–2810.
56. S. Marola, D. Manfredi, G. Fiore, M. G. Poletti, M. Lombardi, P. Fino, L. Battezzati, Journal of Alloys and Compounds, 2018, Volume 742, Pages 271-279.
57. Z. Zhang, D.L. Chen, Materials Science and Engineering: A, 2008, Volumes 483–484, Pages 148-152.
58. Yang, Tao & Wang, Kuaishe & Wang, Wen & Peng, Pai & Huang, Liying & Qiao, Ke & Jin, Yuanyuan, JOM, 2019, 71.
59. Yang, Z.; Fan, J.; Liu, Y.; Nie, J.; Yang, Z.; Kang, Y., 2021, Materials 14, 1219.
60. A.K. Gupta, D.J. Lloyd, S.A. Court, Materials Science and Engineering: A, Volume 316, Issues 1–2, 2001, Pages 11-17.
61. Aboulkhair, N.T., Tuck, C., Ian Ashcroft, Ian Maskery & Nicola M. Everitt, Metall Mater Trans A, 2015, 46, 3337–3341.
62. L. Girelli, M. Tocci, M. Gelfi, A. Pola, Materials Science and Engineering: A, 2019, Volume 739, Pages 317-328.
63. E. Brandl, U. Heckenberger, V. Holzinger, D. Buchbinder, Materials & Design, 2012, Vol. 34 pp. 1